The Astrophysical Journal, 743:70 (7pp), 2011 December 10 doi:10.1088/0004-637X/743/1/70

THE EFFECTS OF PLASMA BETA AND ANISOTROPY INSTABILITIES ON THE DYNAMICS OF RECONNECTING MAGNETIC FIELDS IN THE HELIOSHEATH

K. M. Schoeffler, J. F. Drake, and M. Swisdak
Institute for Research in Electronics and Applied Physics, University of Maryland, College Park, MD 20742-3511, USA
Received 2011 July 27; accepted 2011 October 21; published 2011 November 22

ABSTRACT

The plasma β (the ratio of the plasma pressure to the magnetic pressure) of a system can have a large effect on its dynamics as high β enhances the effects of pressure anisotropies. We investigate the effects of β in a system of stacked current sheets that break up into magnetic islands due to magnetic reconnection, which is analogous to the compressed heliospheric current sheet in the heliosheath. We find significant differences between systems with low and high initial values of β. At low β, growing magnetic islands are modestly elongated and become round as contraction releases magnetic stress and reduces magnetic energy. At high β, the increase of the parallel pressure in contracting islands causes saturation of modestly elongated islands as island cores approach the marginal firehose condition. Only highly elongated islands reach finite size. The anisotropy within these islands prevents full contraction, leading to a final state of highly elongated islands in which further reconnection is suppressed. The elongation of islands at finite β is further enhanced by reducing the electron-to-ion mass ratio to more realistic values. The results are directly relevant to reconnection in the sectored region of the heliosheath where there is evidence that elongated islands are present, and possibly to other high-β systems such as astrophysical accretion flows and the magnetosphere of Saturn.

Key words: instabilities – magnetic reconnection – methods: numerical – plasmas – Sun: general – Sun: heliosphere

Online-only material: color figures

1. INTRODUCTION

At the outer edges of the solar system, the solar wind pushes up against the interstellar medium. Since the solar wind is moving at supersonic speeds, it forms a shock known as the termination shock. The region between the termination shock and the interstellar medium is referred to as the heliosheath. Flapping of the heliospheric current sheet produces sectored magnetic fields (Smith 2001) that have a significant latitudinal extent. There has been research suggesting that the current sheets between the sectored fields found in the heliosheath are compressed to the point that collisionless reconnection begins to occur, resulting in the formation of magnetic islands (Drake et al. 2010; Czechowski et al. 2010). A turbulent magnetohydrodynamic (MHD) model of the reconnection of the sectored fields has also been proposed (Lazarian & Opher 2009) although we will argue later that the *Voyager* data are inconsistent with this hypothesis.

An important question, however, is whether the conventional treatment of collisionless reconnection (Shay et al. 2007) is valid in the heliosheath, where it was suggested that the pick-up ion (PUI) population increases the plasma pressure compared with values at 1 AU (Zank 1999; Richardson et al. 2008; Wu et al. 2009). Although both *Voyager* spacecraft are currently taking data in the heliosheath, the energy range of the detectors does not cover the PUIs, so it is difficult to make a reliable estimate of the value for β, the ratio of the plasma pressure to the magnetic pressure (Richardson et al. 2008). Global MHD simulations suggest, however, that β varies from 8 to 0.5 between the termination shock and the interstellar medium with the highest β just downstream of the termination shock (Drake et al. 2010). Although this simulation does not include a separate PUI population, it provides a rough estimate for the expected values for β and motivates the range of β in our study. In this study, we investigate the impact of β on the dynamics of reconnection and the formation of magnetic islands relevant to the sectored heliosheath.

To begin reconnection and island formation a current sheet needs to be compressed to approximately the ion inertial scale $d_i = c/\omega_{\rm pi}$, where c is the speed of light and $\omega_{\rm pi}$ is the ion plasma frequency (Cassak et al. 2005; Yamada 2007). At this point, the current sheet becomes unstable to the collisionless tearing mode. Upstream of the termination shock the heliospheric current sheet has a thickness of around 10,000 km (Smith 2001) and is predicted to compress to around 2500 km just downstream of the shock. In the upstream region the plasma density measured at *Voyager 2* is around 0.001 $\rm cm^{-3}$, corresponding to an ion skin depth of around 7200 km. In the downstream region the density is compressed to around 0.003 $\rm cm^{-3}$, corresponding to an ion skin depth of around 4200 km. Thus, the compression of the current sheets across the termination shock should trigger collisionless reconnection in the heliosheath and some *Voyager 1* and *2* observations support this hypothesis (Opher et al. 2011).

In our system we will be examining symmetric current sheets with no guide field (initial out-of-plane magnetic field). In an analytic study, Brittnacher et al. (1995) showed that when $\rho_i/w_0 \approx 1$, the fastest growing linear mode occurs at $kw_0 \approx 0.5$, where k is the wavenumber of the tearing mode, w_0 is the half-width of the current sheet, and ρ_i is the ion gyroradius. Since $\rho_i = \sqrt{\beta_i} d_i$, where β_i is the plasma beta based on the ion pressure, the current sheet thickness is comparable to that in our simulation.

Due to the collisionless nature of the plasma, pressure anisotropies ($P_\parallel \neq P_\perp$, where $\parallel$ and $\perp$ are determined with respect to the magnetic field) can form during reconnection. Fermi acceleration in contracting islands (Drake et al. 2006) and adiabatic cooling as B decreases due to conservation of the magnetic moment $\mu \propto v_\perp^2/B \propto P_\perp/B$ both drive $P_\parallel > P_\perp$.

When an anisotropy is formed with $P_\parallel > P_\perp$ the tension in bent magnetic fields weakens. The fluid momentum equation with an anisotropy becomes

$$\rho \frac{d\mathbf{v}}{dt} = -\nabla\left(P_\perp + \frac{1}{8\pi}B^2\right) + \nabla\cdot\left[\left(1 - \frac{\beta_\parallel - \beta_\perp}{2}\right)\frac{\mathbf{BB}}{4\pi}\right], \quad (1)$$

where ρ is the mass density of the plasma, $\mathbf{v}$ is the bulk velocity, and $\mathbf{B}$ is the magnetic field. For $\beta_\parallel = \beta_\perp$ the pressure equation reduces to the standard MHD equation. When $\beta_\parallel > \beta_\perp$ the tension force is reduced. At high β, this reduction of tension force is noticeable for even slight anisotropies in the pressure. For $\beta_\parallel - \beta_\perp$ large enough, the tension force drops to zero, or even becomes negative. Since the tension of field lines acts as a restoring force for Alfvén waves in standard MHD, the negative sign causes this oscillation to become an instability known as the firehose instability (Parker 1958) for

$$\beta_\parallel - \beta_\perp > 2. \quad (2)$$

This instability is fueled by the free energy contained in the pressure anisotropy. The firehose instability causes magnetic field lines to kink, which eventually relieves the pressure anisotropy by causing scattering.

Alternatively, when $\beta_\parallel - \beta_\perp$ is negative and large enough in magnitude, other instabilities can occur. The mirror-mode instability and the ion cyclotron instability both occur when $P_\perp > P_\parallel$. For larger $\beta_\parallel$ the mirror mode becomes unstable at smaller values of $|\beta_\parallel - \beta_\perp|$ than the ion cyclotron mode, so the marginal mirror-mode criterion acts as the boundary between the stable and unstable regions. Based on fluid theory assuming $T_e = T_i$ (Hasegawa 1969), the mirror-mode instability occurs when

$$\beta_\perp - \beta_\parallel > \frac{\beta_\parallel}{\beta_\perp}. \quad (3)$$

There are also kinetic modifications that can be made to the marginal instability criteria for firehose, mirror mode, and ion cyclotron which make them more accurate. Although a rigorous analytic theory is not available, there are models that approximate the instability very well (Hellinger et al. 2006; Bale et al. 2009). However, for simplicity we will just consider the conditions based on fluid theory.

In this study, we simulate several stacked current sheets similar to the compressed sectored heliospheric fields and associated current sheets, and follow the development of reconnection and islands. We implement this system in a two-dimensional particle-in-cell (PIC) code and vary the temperature of the background plasma to test the dependence on β. We observe that in finite β_e systems ($\beta_e > 0.5$), very elongated islands form as opposed to the modest-aspect-ratio islands found at low β_e ($\beta_e < 0.5$), where β_e is the β based on the electron pressure. At high β, the increased $P_\parallel$ due to the Fermi reflection of electrons within islands saturates the normal modest-aspect-ratio islands. Fermi reflection in highly elongated islands is less efficient because of the increased bounce time of the electrons so these islands are able to reach finite amplitude. At late time, however, even these elongated islands exhibit anisotropy instabilities, from Fermi reflection of both ions and electrons. As a result, late-time magnetic islands remain highly elongated and do not become round as in the low-β regime. This result has significant implications for the structure of islands that would be measured in the heliosheath. Although β_e is rather moderate in the heliosheath, we find a mass ratio dependence suggesting long islands for a broad range of β_e in realistic mass ratios. A large β, however, may be necessary to sustain the elongation of these islands.

2. COMPUTATIONAL MODEL

Our simulations are performed with the PIC code p3d. The initial conditions consist of eight Harris current sheets (Harris 1962) where the magnetic pressure balances the plasma pressure. Each Harris sheet consists of a $\tanh(y/w_0)$ and $\mathrm{sech}^2(y/w_0)$ profile along the $\hat{\mathbf{y}}$ direction for an $\hat{\mathbf{x}}$-directed magnetic field and the density, respectively. The peak density of the Harris sheets is n_0. In addition, there is a uniform background population that has a density of $n_b = 0.2n_0$. These simulations are done in two dimensions so $\partial/\partial z = 0$, where $\hat{\mathbf{z}}$ is out-of-plane, parallel to the initial current.

The code uses normalized units. The timescale is normalized to the ion cyclotron time $\Omega_{\rm ci}^{-1}$. The distance scales are normalized to the ion inertial length $d_i = c/\omega_{\rm pi}$. Thus, the velocity is normalized to the Alfvén speed v_A. The magnetic field is normalized to the asymptotic value of the reversed magnetic field B_0. The density is normalized to n_0. The pressure is normalized to $P_0 = n_0 m_i v_A^2 = B_0^2/4\pi$. The temperature is normalized to $T_0 = m_i v_A^2$.

In order to vary the β of these simulations we vary the temperature of the background population T_b. This background temperature is the same for both ions and electrons. The Harris equilibrium is used to balance the sharp change in the magnetic field strength across the current sheets, while the background represents the PUIs and has the greatest influence on late-time reconnection dynamics. We performed simulations for $\beta = 0.2$, 1, 2, 3, and 4.8, where β is based on the pressure in the asymptotic field with density n_b. Each simulation was advanced for a time of $120\Omega_{\rm ci}^{-1}$ with a time resolution $dt = 0.004\Omega_{\rm ci}^{-1}$. The simulations are on a $204.8d_i \times 102.4d_i$ domain with a grid scale resolution of $\Delta_x = \Delta_y = 0.05d_i$. In order to complete such large runs, unless otherwise specified, we used 25 for the mass ratio of the ions to electrons. This makes it easier to resolve small electron scales. In order to lessen the separation between the field and particle timescales, we set the ratio of the speed of light to the Alfvén speed, c/c_A, to 25 (in the heliosheath a more realistic value is near 6000). Reconnection is insensitive to the value of c/c_A. We start with a half-thickness for the current sheet $w_0 = 0.5d_i$, so that collisionless reconnection can begin from particle noise. The temperature in the Harris sheet is $0.25T_0$ for both ions and electrons, and there is no guide field. The largest β we simulated was 4.8 since the electron thermal velocity $v_{\rm the} \approx 0.7c$. Larger β would begin to have significant unphysical relativistic effects, due to our lowered ratio of c/c_A.

The simulation does not precisely describe the heliosheath but illustrates important physics that should be found there. The ion pressure in the heliosheath is much larger than the electron pressure, and thus β_e is actually quite moderate. However, we will show that at realistic mass ratios we still expect elongated islands. The large β, mostly due to ion pressure, is however significant because it allows the elongation to persist. We do not have a separate population of PUIs, and the magnetic field configuration is a Harris sheet rather than the rotated fields (where $|B|$ is constant in a cut through the current sheet) found in the heliosheath. Future simulations tailored to the specific parameters of the heliosheath may help our understanding of this phenomenon.

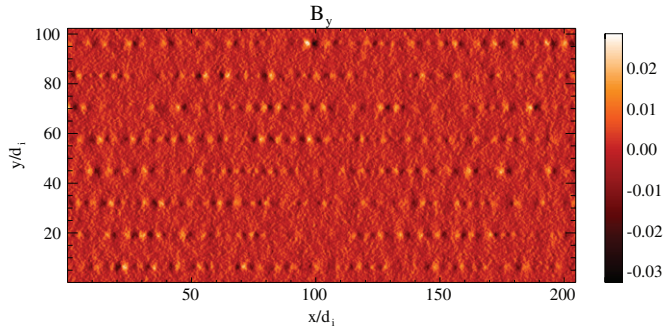

Figure 1. Normal component of the magnetic field, B_y, for $\beta = 2$ at $t = 15\Omega_{ci}^{-1}$. The bipolar signatures in the current sheet indicate the presence of x-lines arising from the collisionless tearing mode.

(A color version of this figure is available in the online journal.)

3. RESULTS

The early development of a run with $\beta = 2$ is shown in Figure 1. Not surprisingly a wave mode with $k_x w_0 \approx 0.5$ clearly emerges. The finite β background plasma does not have a strong effect on the wavelength of linear tearing. During this time, within the current sheets, an anisotropy in the electron pressure begins to develop with $P_{e\parallel} > P_{e\perp}$. The electrons moving at the thermal velocity are able to bounce between the two ends of the islands which have lengths of $\sim 6d_i$. Comparisons with runs at different β show that at this early time, the lengths of the islands appear to be insensitive to β.

There are two important timescales controlling the dynamics: the time it takes for the ions to accelerate to Alfvénic outflow speeds and the time it takes for a significant electron pressure anisotropy to develop. If electrons bounce several times between the two ends of a contracting island, an anisotropy develops which approaches the firehose instability boundary. This is because the bouncing electrons gain energy in the parallel direction. The time for an electron to bounce off the edge of an island and then return to its original position is thus a measure of the time for significant anisotropy to develop.

The tearing instability is driven by the tension in the newly reconnected magnetic fields. Since anisotropies cause a weakening of the magnetic tension, the tearing mode can be suppressed by strong anisotropy within an island.

Reconnecting magnetic field lines, by relaxing their tension, accelerate ions up to Alfvénic speeds. If several bounces occur during the time required for ions to be accelerated up to the Alfvénic outflow speed from the x-line, the developing anisotropy slows the ion outflow and essentially stops the growth of the tearing mode. However, since the bounce time is proportional to the length of the islands, the growth of sufficiently long-wavelength tearing modes can continue.

Near an x-line adjacent to a growing island, the outflow velocity of ions, to first approximation, linearly increases with distance (see Figure 2) as

$$v_{ix} = \frac{1}{t_a} x. \tag{4}$$

At this point, t_a is just defined as the inverse slope of the relationship between v_{ix} and x. Since according to Figure 2 the slope is constant, this implies that ions accelerate away from the x-line in an exponential fashion. By integrating, the time, t, for an ion to accelerate from the initial position, x_0, to the final

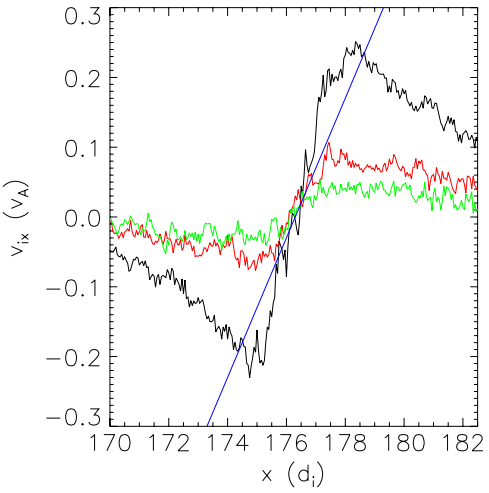

Figure 2. Ion outflow velocity, v_{ix}, vs. the position x, for $t = 25\Omega_{ci}^{-1}$ (green), $30\Omega_{ci}^{-1}$ (red), and $35\Omega_{ci}^{-1}$ (black) for the $\beta = 2$ run. To reduce noise we do a five-point smoothing of v_{ix} in both the $\hat{\mathbf{x}}$ and $\hat{\mathbf{y}}$ directions. The blue curve is a line of slope 0.1, which corresponds to a convective growth time t_a of around $10\Omega_{ci}^{-1}$.

(A color version of this figure is available in the online journal.)

position, x_f, can be obtained:

$$t = \int_{x_0}^{x_f} \frac{dx}{v_{ix}} = \int_{x_0}^{x_f} \frac{t_a dx}{x} = t_a \ln \frac{x_f}{x_0}, \tag{5}$$

and thus

$$x_f = x_0 e^{t/t_a}. \tag{6}$$

An approximate measure for the characteristic timescale for acceleration away from the x-line up to the Alfvén speed is $t \approx t_a$, the acceleration time. As seen in Figure 2, the acceleration time at $t = 30\Omega_{ci}^{-1}$ is of order $\sim 10\Omega_{ci}^{-1}$. This acceleration time is approximate, can vary by a factor of as much as two, and appears to be insensitive to β.

The bounce time can be estimated based on the thermal velocity of the electrons, v_{the}, and the length of the island, L:

$$t_b = \frac{L}{v_{the}} = \frac{L}{v_A}\sqrt{\frac{1}{\beta_e}\frac{m_e}{m_i}}, \tag{7}$$

where β_e is the β determined solely from the plasma pressure derived from the electrons.

Equating the empirical acceleration time $t_a = 10\Omega_{ci}^{-1}$, and the bounce time t_b, Equation (7), a critical island length can be found:

$$L_{crit} \approx 10 d_i \sqrt{\beta_e \frac{m_i}{m_e}}. \tag{8}$$

For islands with $L < L_{crit}$, the anisotropy will stop the tearing instability. Islands smaller than L_{crit} can still form, but they quickly saturate. A similar saturation was found in Karimabadi et al. (2005). However, in their simulations the size of the computational domain was $12.6\rho_i$ and $L_{crit} = 100\rho_i$, where ρ_i is the ion Larmor radius. Thus, the development of long-wavelength islands was not observed.

For the case of $\beta = 2$ ($\beta_e = 1$) and $L \approx 6d_i$, $t_b \approx 1.2\Omega_{ci}^{-1}$. This time is much less than the acceleration time, so there is enough time for a significant anisotropy to develop before a significant x-line is established. This anisotropy can be seen in Figure 3(a), which shows the regions from the $\beta = 2$

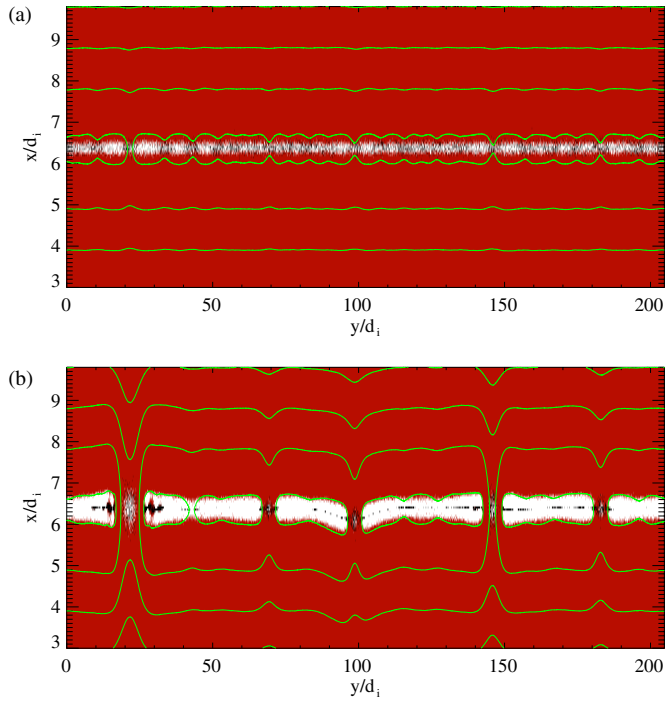

Figure 3. Regions where the plasma anisotropy causes instability. White regions are unstable to the firehose, black regions are unstable to the mirror mode, and red are stable. The green lines are magnetic field lines. This plot shows one current layer taken from the $\beta = 2$ run at (a) $t = 25\Omega_{ci}^{-1}$ and (b) $t = 40\Omega_{ci}^{-1}$. The aspect ratio is distorted to make the islands more visible.

(A color version of this figure is available in the online journal.)

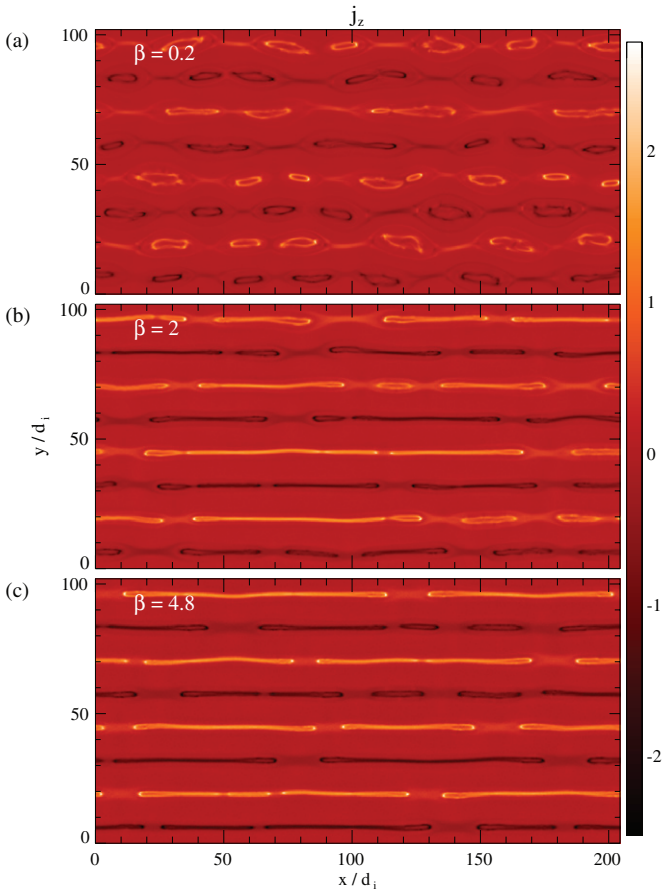

Figure 4. Out-of-plane current, j_z, at $t = 51\Omega_{ci}^{-1}$ for β of (a) 0.2, (b) 2, and (c) 4.8.

(A color version of this figure is available in the online journal.)

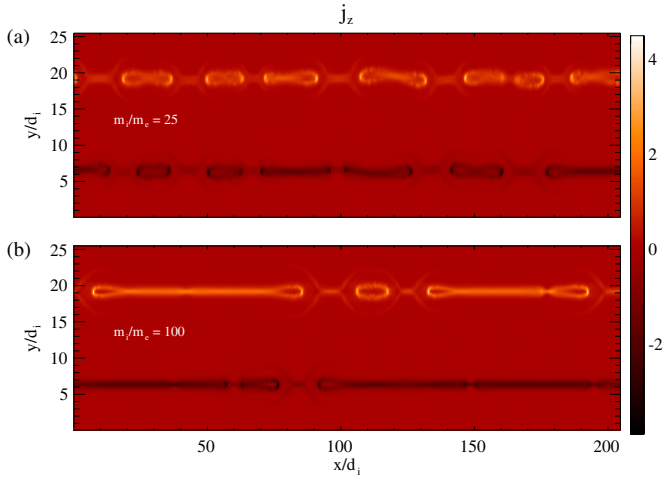

Figure 5. Out-of-plane current, j_z, for $\beta = 0.2$ at (a) $t = 40\Omega_{ci}^{-1}$ for $m_i/m_e = 25$ and (b) $t = 60\Omega_{ci}^{-1}$ for $m_i/m_e = 100$. The aspect ratio is distorted to make the islands more visible.

(A color version of this figure is available in the online journal.)

run that are unstable to the firehose instability. The unstable regions occur inside the islands and stop further growth of the short-wavelength tearing modes. The islands that continue to grow correspond to longer wavelength, with $L \approx 40d_i$ and $t_b \approx 8\Omega_{ci}^{-1} \approx t_a$. Thus, the anisotropy develops slowly enough for reconnection to develop. This can be seen in Figure 3(b).

As can be seen in Figure 4, by $t = 51\Omega_{ci}^{-1}$, β has a significant influence on the structure of islands. The islands for $\beta = 0.2$ have much shorter wavelength than for $\beta = 2$ and 4.8. In other words, there are more locations where reconnection proceeds in the case of low β. This phenomenon is expected based on the previous analysis, $L_{crit} \propto \sqrt{\beta_e}$. Since L_{crit} is proportional to the square root of the mass ratio $\sqrt{m_i/m_e}$, we expect to find much longer islands in the real mass ratio limit. To test this, we perform a $\beta = 0.2$ simulation with $m_i/m_e = 100$. In this case, we reduce the y-domain by a factor of four with respect to Figure 4(a), examining only two current sheets. We double the resolution in order to resolve the small electron scales and reduce the ratio of the speed of light to the Alfvén speed to 15. There is a clear dependence on m_i/m_e shown in Figure 5, where we compare the bottom two current sheets of Figure 4(a) to the new simulation. We find the islands to be significantly longer, confirming our prediction. Since $m_i/m_e \gg 100$ in the heliosphere, long islands are almost always expected, unless β_e is very small.

As elongated islands grow at high β, anisotropies within them also develop even though the anisotropies do not suppress island growth. The anisotropy surpasses the firehose condition in the center of the islands. These anisotropies are likely caused by the Fermi mechanism (Drake et al. 2006). The dynamics of this acceleration mechanism will be discussed in a future paper. The contraction of islands can be seen in Figure 6. The higher density regions inside of the islands move inward at Alfvénic speeds. At around $t = 61$–$66\Omega_{ci}^{-1}$ the islands begin to kink, which indicates the onset of an anisotropy instability.

The short-wavelength mode is caused by the temperature anisotropy due to the outflow from the x-line streaming through the plasma entering the exhaust across the separatrix and the

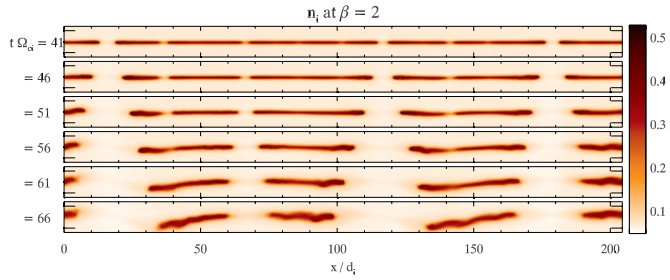

Figure 6. Ion density, n_i, for $\beta = 2$ along one current sheet between $t = 41$ and $66\Omega_{ci}^{-1}$.

(A color version of this figure is available in the online journal.)

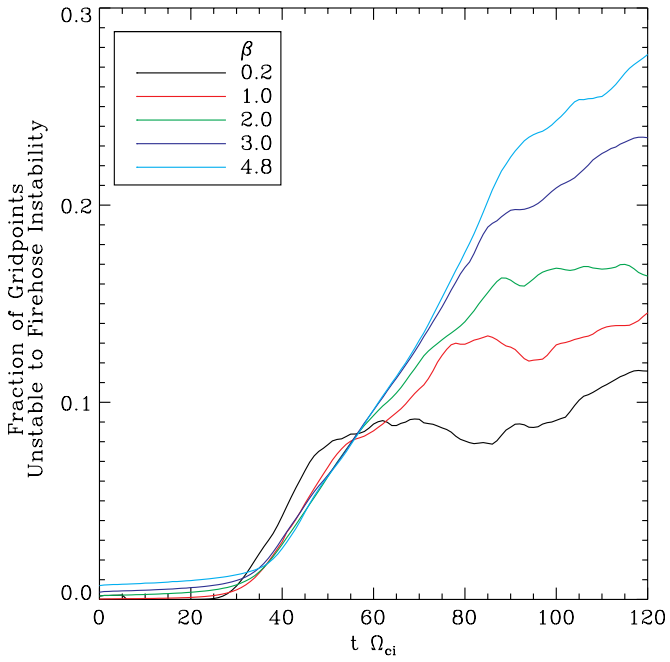

Figure 7. Fraction of grid points unstable to the firehose instability vs. time for $\beta = 0.2$, 1, 2, 3, and 4.8.

(A color version of this figure is available in the online journal.)

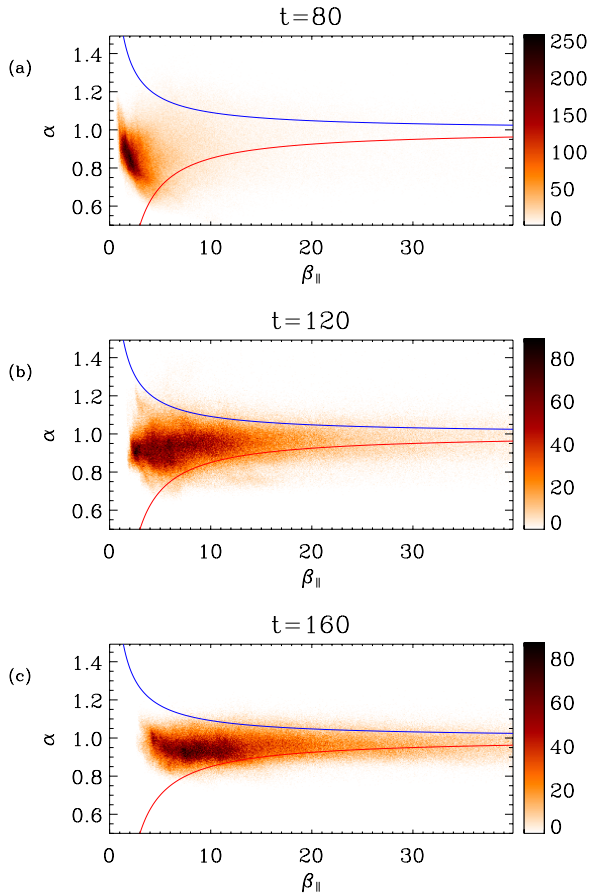

Figure 8. Two-dimensional histogram of anisotropy ($\alpha = P_\perp/P_\parallel$) vs. $\beta_\parallel$ for $\beta = 2$ at times from top to bottom $t = 80$, 120, and $160\Omega_{ci}^{-1}$. The blue line represents the marginal condition for mirror-mode instability. Points above this curve are unstable. The red line represents the firehose marginal stability condition. Points below this curve are unstable. The color bar represents the number of points with a particular α and $\beta_\parallel$.

(A color version of this figure is available in the online journal.)

Fermi acceleration of electrons bouncing in the island. Based on the similarities in growth rate and other signatures that will be discussed in a future paper, this mode appears to be associated with the Weibel instability.

The anisotropies that develop during the reconnection simulation do not grow without bound. In Figure 7, we plot the fraction of grid points that are unstable to the firehose instability. As time advances and the anisotropies begin to form, the number of grid points unstable to the firehose instability increases. However, at $t \sim 80\Omega_{ci}^{-1}$, the number of unstable grid points begins to saturate. Since it takes place soon after the onset of the kinking of the islands, the saturation is likely because the anisotropy is reduced via scattering by the Weibel and firehose instabilities. Additionally, the saturation occurs soon after the unreconnected flux is exhausted. By $60\Omega_{ci}^{-1}$ the islands have grown enough so that the islands on adjacent current sheets begin to interact. This is an additional reason for the saturation of the firehose unstable area: there is no more space into which the firehose unstable islands can expand.

At late time, the anisotropy of the system is confined within the boundaries of the marginal firehose (Equation (2)) and mirror-mode instabilities (Equation (3)) in a manner similar to that seen in observations of the solar wind (Hellinger et al. 2006; Bale et al. 2009) and in earlier low-β current sheet simulations (Drake et al. 2010). Figure 8 shows the data for our system in the space of (α,$\beta_\parallel$) where $\alpha = P_\perp/P_\parallel$. This plot is generated by calculating the anisotropy α and the $\beta_\parallel$ for each grid point. The plot is a two-dimensional histogram of grid points in (α,$\beta_\parallel$) space, where $\beta_\parallel$ is calculated based on $P_\parallel$. The parallel and perpendicular pressures are calculated by taking the diagonal components of the pressure tensor after rotating into the frame of the local magnetic field, such that the two perpendicular components are equal. We look at the distribution at $t = 80$, 120, and $160\Omega_{ci}^{-1}$. At early times, the anisotropies have not yet fully developed and the plasma still occupies a small region in (α,$\beta_\parallel$) space. By $t = 120\Omega_{ci}^{-1}$, the anisotropy has reached the two stability boundaries and continues to be confined between these two boundaries at $t = 160\Omega_{ci}^{-1}$, even as the average β increases. The anisotropy reaches the stability boundaries at a time after the short-wavelength Weibel modes have dissipated. Since at this point there are no longer large regions with essentially zero magnetic fields, the firehose and mirror-mode instabilities are what determine the boundaries of the temperature anisotropies. There are no clear signatures of the classical mirror-mode instability at this time. The firehose and mirror-mode instabilities may be hard to distinguish among the turbulent interacting magnetic islands, or the islands may

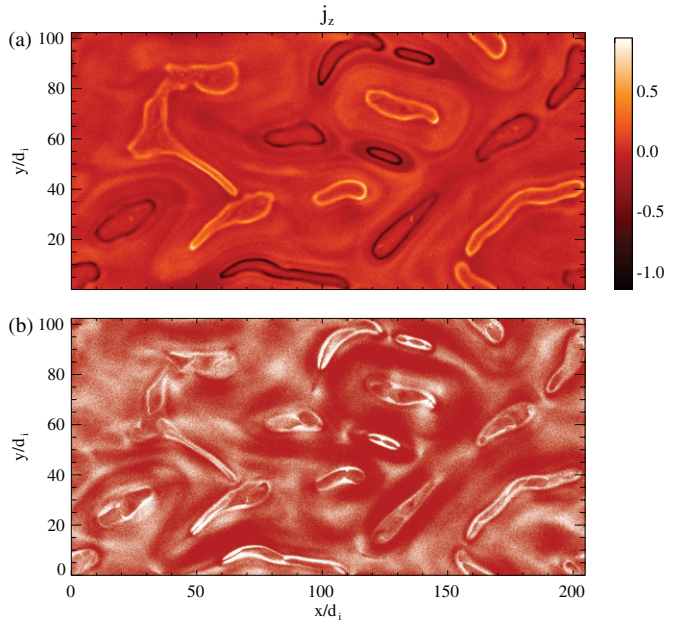

Figure 9. Out-of-plane current, j_z (a), and stability (b) at $t = 120\Omega_{ci}^{-1}$ for the $\beta = 4.8$ case. White regions in part (b) are unstable to the firehose, and red are stable.

(A color version of this figure is available in the online journal.)

just stop generating anisotropy as they approach the instability boundaries.

The islands maintain an elongated form for the simulation shown in Figure 4(c) clear until $t = 120\Omega_{ci}^{-1}$, the latest time simulated for $\beta = 4.8$. This is shown in Figure 9(a) showing the out-of-plane current for $t = 120\Omega_{ci}^{-1}$. Since the edges of the islands are pushing against the firehose instability, the tension force in the magnetic fields is eliminated. This can be seen in Figure 9(b) which shows the regions that are unstable to the firehose instability.

4. CONCLUSIONS

The magnetic islands that reach a significant amplitude are much more elongated at high β_e than at low β_e. These elongated islands should be found even for moderate values of β_e at realistic mass ratios. Island elongation is caused by the suppression of the shorter wavelength tearing modes by pressure anisotropies ($P_\parallel > P_\perp$) that develop due to the Fermi acceleration of electrons. Later in time the plasma develops pressure anisotropies of both ions and electrons that are limited by the firehose and Weibel instabilities. A Weibel mode develops that kinks the magnetic field lines. In the regime with a real mass ratio we would expect even longer islands to form, where multiple wavelengths of the firehose instability could develop. At late time, the fraction of points unstable to the firehose instability saturates, and the anisotropy is confined between the mirror mode and firehose instability boundaries. The long islands persist due to the low requirement of anisotropy to reach the marginal firehose condition at high β. For even small anisotropies the tension in the magnetic fields is removed.

When encountering magnetic islands in the heliosheath, we predict the formation of similar extended, sausage-shaped islands rather than the more round islands found in low-β simulations (Drake et al. 2010). The cores of these islands should also be at the marginal firehose condition, so the magnetic tension that drives them to become round vanishes. We would

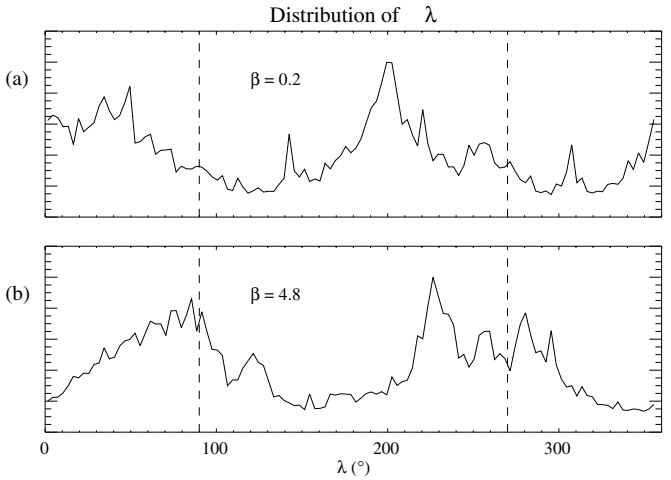

Figure 10. Distribution of λ at $t = 110\Omega_{ci}^{-1}$ for the (a) $\beta = 0.2$ case and (b) $\beta = 4.8$ case. The dotted lines are at $\lambda = 90^\circ$ and 270° where we expect to find peaks in the distribution.

thus expect these sausage shapes to persist long after the islands have ceased growing, and thus could be found even in regions where reconnection is no longer occurring.

These elongated islands exhibit signatures that can be seen in *Voyager* data. In particular, *Voyager* measures all three components of the magnetic field. Of particular interest for the explorations of islands that grow in the ecliptic plane is the angle $\lambda = \tan^{-1}(B_T/B_R)$, where B_T and B_R are the azimuthal and radial magnetic fields, respectively. $\lambda = 90^\circ$ and 270° correspond to the azimuthal unreconnected sectored heliosheath magnetic fields. Deviation of λ from 90° and 270° indicates some process is distorting the sectored field. *Voyager* data show the distribution of λ is peaked in the two azimuthal directions, $\lambda = 90^\circ$ and 270° (Opher et al. 2011). These peaks are significantly broader in the heliosheath than upstream, indicating that reconnection or another mechanism is disturbing the heliosheath field. The observed *Voyager* distribution of λ is consistent with that found in high-β simulations (Opher et al. 2011). Since the islands are elongated, the magnetic fields tend to remain primarily in the azimuthal direction even well after the islands begin to interact with each other. Round islands, such as would be expected from an MHD model or a low-β kinetic model, are not consistent with observations since they produce much broader λ distributions. Thus, MHD reconnection (Lazarian & Opher 2009) in the heliosheath seems to be ruled out. Shown in Figure 10 is the distribution of λ from the simulations at $\beta = 0.2$ (Figure 4(a)) and $\beta = 4.8$ (Figure 4(c)) at $t = 110\Omega_{ci}^{-1}$. The high-β simulation which has elongated islands retains the two peaks at $\lambda = 90^\circ$ and $\lambda = 270^\circ$. The long islands have a larger magnetic field in the azimuthal direction than the radial, resulting in peaks in the λ distribution, but the shorter islands become round having a magnetic field with similar strength in both directions, resulting in a broad distribution in λ. The loss of tension in a finite β plasma prevents the complete release of magnetic energy that would be expected in an MHD model. A complete understanding of the β dependence of magnetic islands is essential in order to obtain reliable signatures that can be compared with *Voyager* data.

In this work there was no out-of-plane guide magnetic field. In the heliospheric current sheet, the magnetic field rotates from one direction to the other keeping a constant magnitude rather than passing through zero (Smith 2001). A guide field would

cause the center of the islands to have a much lower β since the magnetic field does not go to zero. Because of this magnetic field, we would not expect the Weibel instability to develop. In real systems there is frequently a guide field, so this would be worth further investigation.

In astrophysical accretion disks, reconnection plays a role in determining the saturation of the magnetorotational instability (MRI; Sano et al. 2004). The saturation of MRI is strongly dependent on the dissipation of the magnetic field due to reconnection. For the high β in accretion disks, suppression of the most strongly growing small islands may significantly impact the saturation of the MRI. Since β is typically larger than 100 in these structures, the only surviving islands would be so long that it is likely that much of the magnetic free energy would not be dissipated. Further, since the MRI requires magnetic tension, the absence of tension could limit the development of the instability. Sharma et al. (2006) perform a simulation showing an enhancement of the growth of MRI due to anisotropies with $P_\perp > P_\parallel$, which enhances the magnetic tension, caused by μ conservation as a magnetic field develops. They do not capture the physics of reconnection and Fermi acceleration in magnetic islands that would generate anisotropies with $P_\perp < P_\parallel$, which removes magnetic tension. These two competing sources of anisotropy, both affect the tension and thus the growth of the MRI. The relative importance of these mechanisms needs to be explored.

Reconnection at high β, although relatively rare in the terrestrial magnetosphere, is also found in the magnetosphere of Saturn (A. Masters et al. 2011, in preparation). Magnetic islands were discovered in a region where β is larger than 10. The β dependence of the growth of finite-sized magnetic islands may lead to a better understanding of these findings.

Since the development of elongated islands requires only moderate β, we expect to see the development of longer islands than expected in lower β systems such as the magnetosphere. In contrast to Karimabadi et al. (2005), these longer islands can grow to a large enough size to play a role in magnetospheric dynamics. Since the β of the magnetosphere is not exceptionally large, it is unlikely that the persisting anisotropy is enough to keep the islands from eventually becoming round.

The computations were performed at the National Energy Research Scientific Computing Center. This work has been supported by NSF grant ATM-0903964 and NASA grant NNG06GH23G.

REFERENCES

Bale, S. D., Kasper, J. C., Howes, G. G., et al. 2009, Phys. Rev. Lett., 103, 211101
Brittnacher, M., Quest, K. B., & Karimabadi, H. 1995, J. Geophys. Res., 100, 3551
Cassak, P., Shay, M. A., & Drake, J. F. 2005, Phys. Rev. Lett., 95, 235002
Czechowski, A., Grzedzielski, S., & Strumik, M. 2010, in AIP Conf. Proc. 1216, Twelfth International Solar Wind Conference, ed. M. Maksimovic, K. Issautier, N. Meyer-Vernet, M. Moncuquet, & F. Pantelli (Melville, NY: AIP), 588
Drake, J. F., Che, H., Shay, M. A., & Swisdak, M. 2006, Nature, 443, 553
Drake, J. F., Opher, M., Swisdak, M., & Chamoun, J. N. 2010, ApJ, 709, 963
Harris, E. G. 1962, Nuovo Cimento, 23, 115
Hasegawa, A. 1969, Phys. Fluids, 12, 2642
Hellinger, P., Travnicek, P., Kasper, J. C., & Lazarus, A. J. 2006, Geophys. Res. Lett., 33, L09101
Karimabadi, H., Daughton, W., & Quest, K. B. 2005, J. Geophys. Res., 110, A03214
Lazarian, A., & Opher, M. 2009, ApJ, 703, 8
Opher, M., Drake, J. F., Swisdak, M., et al. 2011, ApJ, 734, 71
Parker, E. N. 1958, ApJ, 128, 664
Richardson, J. D., Kasper, J. C., Wang, C., Belcher, J. W., & Lazarus, A. J. 2008, Nature, 63, 454
Sano, T., Inutsuka, S., Turner, N. J., & Stone, J. M. 2004, ApJ, 605, 321
Sharma, P., Hammett, G., Quataert, E., & Stone, J. 2006, ApJ, 637, 952
Shay, M. A., Drake, J. F., & Swisdak, M. 2007, Phys. Rev. Lett., 99, 155002
Smith, E. J. 2001, J. Geophys. Res., 106, 15819
Wu, P., Winske, D., Gary, S. P., Schwadron, N. A., & Lee, M. A. 2009, J. Geophys. Res., 114, A08103
Yamada, M. 2007, Phys. Plasmas, 14, 058102
Zank, G. P. 1999, Space Sci. Rev., 89, 413